Aerosol Filtration

For aerosol filtration in fibrous media, the ratio of dp/dg is often of the order of 1/10.

From: Principles of Filtration, 2012

Related terms:

Nanoparticles, Polytetrafluoroethylene, Sodium Chloride, Water Filtration, Nanofibers, Aerogel, Differential Mobility Analyzer, Polyimide

Filter testing, filter test standards, and filter ratings

Wallace Woon-Fong Leung ScD (MIT), in Nanofiber Filter Technologies for Filtration of Submicron Aerosols and Nanoaerosols, 2022

4.2.1 Testing grade efficiency

Aerosol filtration efficiency of filters can be evaluated with a submicron aerosol generation system generating monodispersed submicron aerosols in conjunction with a filter test setup. A representative setup is shown schematically in Fig. 4.1 (Leung & Hung, 2008; Sun & Leung, 2019). Sodium chloride (NaCl) is commonly used as a test aerosol. It is generated from atomizing NaCl solution of 0.5%–5% by weight. The generated polydispersed aerosols have electrical charges and are subsequently passed through a membrane dryer where water moisture from atomization is removed from the aerosol stream. Subsequently, the aerosol stream is sent to an impactor where aerosols with sizes larger than 600 nm are removed. The undersize aerosols are then sent to a neutralizer, which is also an ionizer, where the charges are imparted onto the aerosols in the air stream with more charges for larger aerosols and vice versa. Subsequently, the charged aerosol stream is sent to a differential mobility analyzer (DMA) where charged aerosol of a prescribed size is retained by the electric field in the DMA, while other aerosol sizes are being rejected. Using an electric field, the DMA operates the classification of aerosol charge that is directly proportional to the aerosol size. Therefore it is possible to classify aerosols using the DMA according to different aerosol sizes based on the electrical charges or mobility of the aerosol. Subsequently, the aerosol stream is sent to a second ionizer/neutralizer where the charges on the aerosols are adjusted to a Boltzmann distribution with zero net charge. The neutralized monodispersed NaCl aerosols are fed to a test column with the clamped test filter. For example, a test filter with a diameter of 7.0 cm (area 38.5 cm^2) was used to test a nanofiber filter with flow entering the test column at a distance at least 20 times the test column bore diameter (i.e., entry length >1.4 m) to ensure the combined concentrated aerosol stream and make-up air (not shown in Fig. 4.1) get uniformly mixed/homogenized and stabilized before challenging the filter (Leung & Hung, 2008). The test filter can be supported downstream by a sturdy scrim support and be protected upstream from abrasion by a polypropylene substrate with negligible efficiency and pressure drop. The filter samples are tested at a face velocity of 5.3 cm/s using a flow rate of 12.24 L/min for a 7-cm diameter test filter. A commercial filter tester TSI 8130A uses a test filter area of 100 cm^2 with a feed rate of 32 L/min. This also results in a face velocity at the filter of the same magnitude, 5.33 cm/s. The system flow rate is measured with a mass flowmeter at the inlet of the filter test system and an ancillary air source is used to make up the required air flow as the aerosol stream from the DMA only delivers a low flow rate with high

aerosol concentration. Aerosols are extracted isokinetically (i.e., at the same velocity) with sampling probes located, respectively, upstream and downstream of the filter to a condensation particle counter (CPC) that is used to measure aerosol concentrations. Within the upper detection limit of CPC, concentration of each particle size is ensured to be sufficiently high to reduce measurement errors. Such system can facilitate efficiency measurement for an aerosol range of 40–500 nm with high accuracy. For the upstream aerosol flow, the high feed concentration of sodium chloride aerosols needs to be reduced by dilution prior to feeding the CPC.

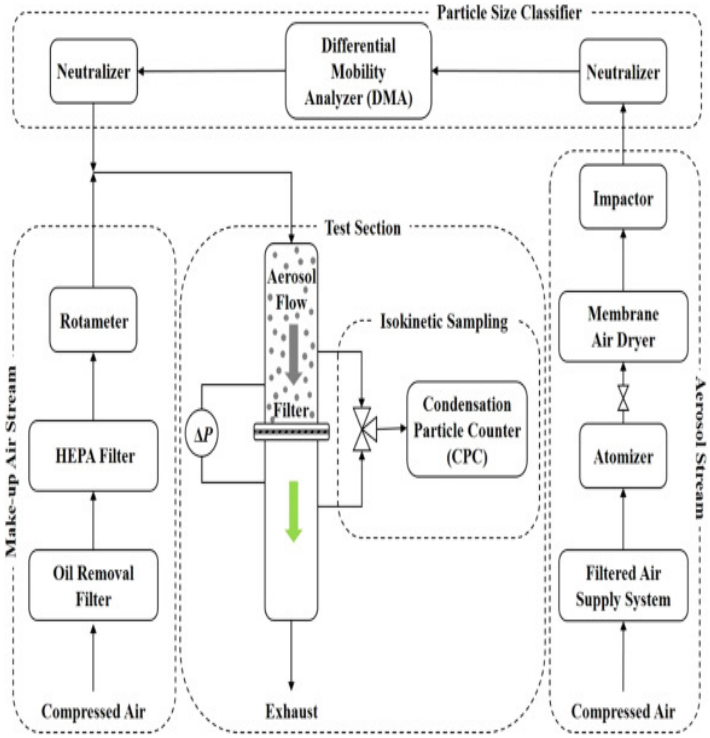

Figure 4.1. Schematic diagram of setup on aerosol efficiency testing of filters (Sun & Leung, 2020). *HEPA*, High efficiency particulate air.

In Fig. 4.1 the pressure drop (ΔP) across the filters is measured using a digital pressure transducer connected across two locations immediately upstream and downstream of the filter, respectively. The following two equations are applicable to calculate filtration efficiency (η) and quality factor (QF, i.e., benefit-to-cost ratio), respectively:

$$\eta = \frac{C_{in} - C_{out}}{C_{in}} \tag{4.1}$$

$$QF = -\frac{\ln(1-\eta)}{\Delta p} \tag{4.2}$$

where C_{in} and C_{out} denote the aerosol number concentrations upstream and downstream of the filter, respectively. Quality factor, QF, in Eq. (4.2) represents a benefit-to-cost ratio for the filter. It has a unit of reciprocal of pressure drop. Usually a filter with high efficiency typically accompanies with higher pressure drop with exception of electrostatic charged filters to be discussed in Chapter 8, Electret Filter for Depth and Cake Filtration. A filter with higher QF represents the efficiency increases at a faster rate than increase in pressure drop, and vice versa.

Fig. 4.2A shows an aerosol size distribution for filtration efficiency tests (Leung & Hung, 2008; Sun & Leung, 2019). The minimum size of the feed distribution is 40 nm with concentration $2.3\times10^3/cm^3$ and maximum size at 500 nm with concentration $<50/cm^3$. The maximum concentration occurs at a size of 80 nm (i.e., the mode of the feed size distribution) with a concentration of $0.6\times10^4/cm^3$. By reducing the NaCl concentration to 0.4% by weight, the minimum aerosol size

with sufficient aerosols concentration for accurate measurements can be extended down to 20 nm (not shown).

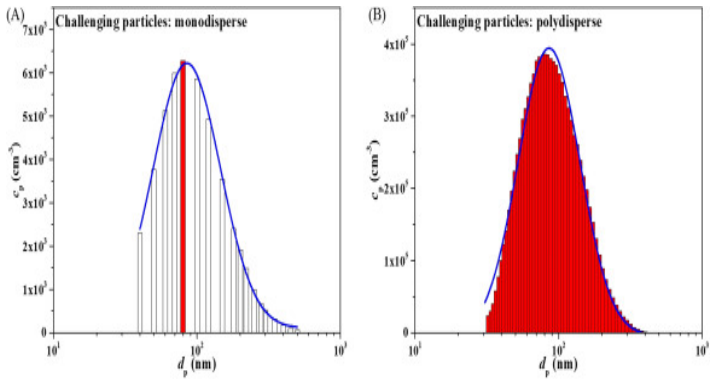

Figure 4.2. Typical diameter distribution of particles for (A) filtration efficiency tests and (B) aerosol loading.

Fibrous Media

Jean-Christophe Appert-Collin, Dominique Thomas, in Aerosol Filtration, 2017

2.4.3 Packing density

Packing density (α) is the ratio of the volume of the fibers to the volume of the fibrous media. In aerosol filtration, the fibrous media largely present packing density values lower than 20–30%. This may be determined using grammage (G), thickness of the media (Z) and the density of fibers (ρ_{Fi}) (equation [2.2]).

$$\alpha = \frac{10^{-3}\, G_{(\text{in g.m}^{-2})}}{Z\, \rho_{Fi}} \qquad [2.2]$$

Packing density determined in this way remains a mean value. A method developed by Bourrous *et al.*[BOU 14] makes it possible to overcome some of the uncertainties linked to the measurement of thickness and weight. This method proposes coating the filtering media in a resin, polishing the edge and observing it through a scanning electron microscope (SEM). Coupling this observation with an energy dispersive X-ray (EDX) analysis of a chemical element characteristic of the fibers (e.g. silicium for glass fibers), it is possible to examine local and average packing density of the zone studied.

This methodology also makes it possible to access the packing density profile in the fibrous media thickness (Figure 2.5). Obtaining a mean value for the packing density of the fibrous media does, of course, require the analysis of a large number of samples.

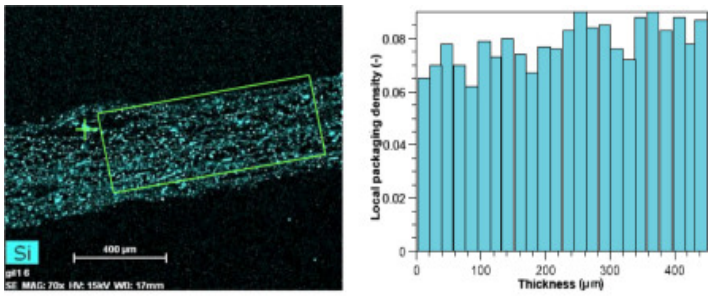

a) b)

Figure 2.5. Using EDX analysis to locally determine packing density. a) EDX cartography of the element silicon in the thickness of a glass fiber media. b) Profile obtained of the packing density of the media. For a color version of this figure, see www.iste.co.uk/thomas/filtration.zip

For some years now, microtomography using X-rays, a non-destructive and non-invasive method, has been widely used to characterize porous media (see the review of Moreno-Atanasio *et al.*[MOR 10]) as it makes it possible to reconstruct a very high-resolution 3D image of the sample analyzed. This technique, based on the difference in attenuation of X-rays (by absorption) by different materials, was notably used by Charvet *et al.*[CHA 11] in order to determine the packing density of a virgin filter (Figure 2.6).

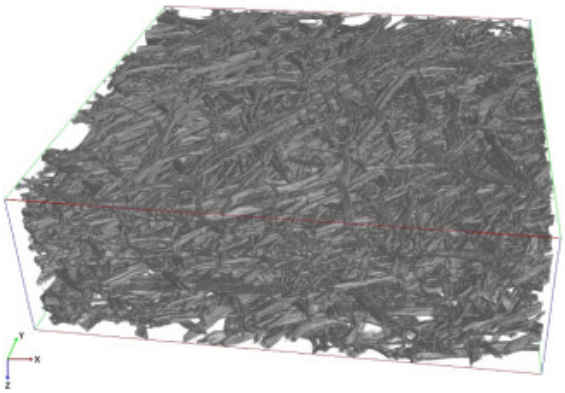

Figure 2.6. *3D visualization of a filter with cellulosic fibers (1,050 × 1,050 × 350 µm); European Synchrotron Radiation Facility, Grenoble, France[CHA 11]*

Read full chapter

URL: https://www.sciencedirect.com/science/article/pii/B9781785482151500020

Cleaning of nanofiber filter

Wallace Woon-Fong Leung ScD (MIT), in Nanofiber Filter Technologies for Filtration of Submicron Aerosols and Nanoaerosols, 2022

10.3 Aerosol distribution in a loaded filter

As discussed in Chapter 6, Transition From Depth-to-Surface Filtration for a Nanofiber Filter, Chapter 7, Cake Filtration With Composite Micro–Nanofiber Filter, Chapter 8, Electret Filter for Depth and Cake Filtration, and Chapter 9, Numerical Modeling of Aerosol Filtration Using a Nanofiber Filter, the aerosols are distributed nonuniformly during the loading of the filter with more aerosols trapped in the filter at the upstream front end of the filter forming a less permeable skin layer, which accounts for the majority of the aerosol deposit and also the pressure drop of the filter. Not only the skin layer increases the airflow resistance, aerosols start depositing on the surface of the filter initiating the formation of an aerosol cake. Over time, as more aerosols deposit on the filter the cake layer increases in thickness, it is possible that the cake layer is nonuniformly packed with finer aerosols infiltrating to the bottom of the cake layer adjacent to

the filter, while larger aerosols deposited and retained near the cake surface. This has been confirmed by the numerical model in Chapter 9, Numerical Modeling of Aerosol Filtration Using a Nanofiber Filter as well as the MERV rating test example discussed in Section 4.13, and loading of the charged single-module filter in Fig. 8.15 that shows consecutive increase in slope of the loading curve during cake filtration. In any event, there is flow resistance that is represented by the pressure drop across the cake as well as across the filter loaded with aerosols. The total pressure drop across the filter and cake may have attributed largely to the aerosol deposit in the cake, especially under extended aerosol loading resulting in a thick cake layer for an uncharged filter, see Chapter 7, Cake Filtration With a Composite Micro-Nanofiber Filter and Chapter 8, Electret Filter for Depth and Cake Filtration. Given the pressure drop across the loaded filter also reflects largely on the amount of cake formed on the filter surface, higher pressure drop indicates a thicker cake. Thus the end point can be set on aerosol loading on a filter by the pressure drop reaching an arbitrary maximum, also referred to as the terminal pressure drop. For the tests discussed next, this maximum pressure drop is being set nominally to 800–850 Pa. Alternatively, one can prescribe a fixed duration for loading the filter and the pressure drop across the filter is monitored continuously until the time limit set on the filter operation has been reached. The maximum pressure attained at the end of fixed duration of aerosol loading typically increases during consecutive loading cycles as more deposited aerosols "plug-up" the pores near the filter surface forming a densely packed residual heel layer.

Loading a test filter using ambient air suffers from uncontrolled aerosols size, concentration distribution, and composition, all of which may also fluctuate over time. It would be very difficult to draw comparison between the different filter configurations as the feed aerosols are changing over an extended test period. To have a better control of aerosol loading on a filter, the PA6 nanofiber filter sample produced from electrospinning is loaded by neutralized polydispersed sodium chloride (NaCl) aerosols generated by a submicron aerosols generator (SMAG) to simulate an accelerated aerosol loading under steady-state controlled condition. The schematic layout of the SMAG for filter loading is depicted in Fig. 10.3.

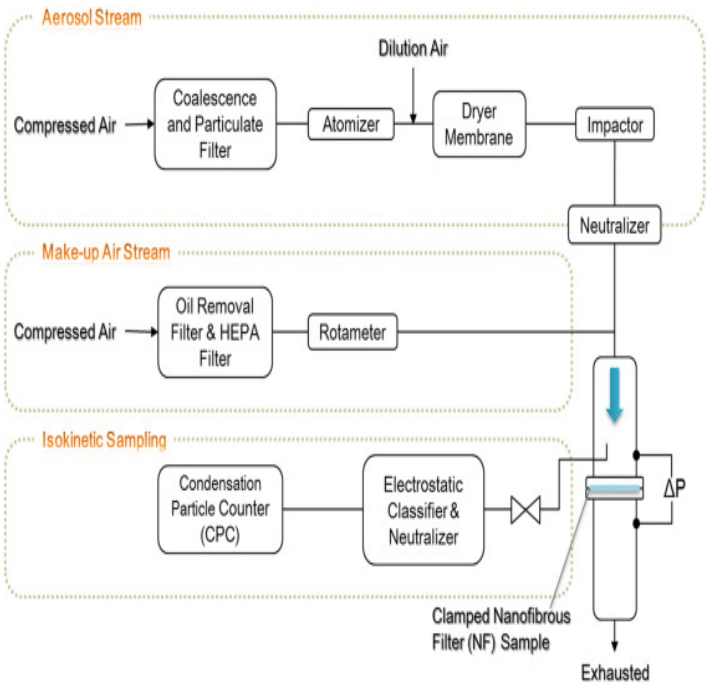

Figure 10.3. Schematic of SMAG and filter testing setup. *SMAG*, Submicron aerosols generator.

The NaCl aerosols that are used to challenge the test filter have size distribution shown in Fig. 10.4. As can be seen, large particles greater than 600 nm are removed. The feed contains, by number concentration, 60% less than 100 nm and

90% less than 160 nm. Indeed, the filter is largely loaded with nanoaerosols (≤100 nm) and submicron aerosols.

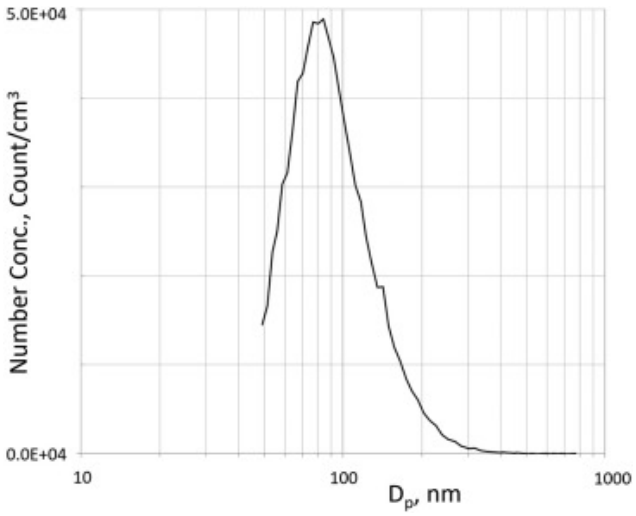

Figure 10.4. Aerosol count concentration per cubic centimeter generated by the SMAG after large particles (>600 nm) are being removed. *SMAG*, Submicron aerosols generator.

Prior to loading the filter, the electrospun nanofiber filter is first tested for the pressure drop and filtration efficiency at a given aerosol flow rate. This is shown in Fig. 10.5A. As an example, Fig. 10.5D shows the grade efficiency for different aerosol sizes (obtained from monodispersed aerosol testing) of a clean nanofiber filter before loading with polydispersed NaCl aerosols. The U-shape behavior of filter efficiency versus aerosol size shows diffusion, interception, and inertial impaction at work in capturing challenging aerosols. The most penetrating particle size (MPPS) is at 150 nm.

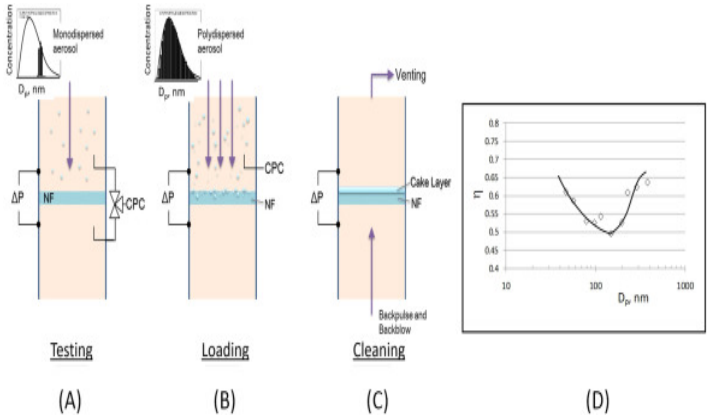

Figure 10.5. Experimental setup of test column for respectively (A) grade efficiency testing, (B) aerosol loading on filter, and (C) filter cleaning. (D) Measured grade efficiency versus aerosol size for a clean filter before aerosol loading.

Read full chapter

URL: https://www.sciencedirect.com/science/article/pii/B9780128244685000207

Raw Materials for Nonwoven Filter Media

Irwin M. Hutten, in Handbook of Nonwoven Filter Media (Second Edition), 2016

4.3.5.5.2 Electrospun webs

Electrospun webs are composed of a nanofiber web structure. There are a number of polymeric materials that used for electrospun nanofiber production. Donaldson

Corporation uses nylon in their Spider Web® and Ultra web® media. Schreuder-Gibson and Gibson (179) in their discussion of electrospun nanofibers for aerosol filtration conducted experiments with polyurethanes and Nylon 6. Formhals (26) conducted his studies with cellulose esters. Choi et al. (180) created electrospun nanofibers from silica using a sol-gel process. Huang et al. (181) identified 44 polymers that have been successfully electrospun from the solution process and 6 from the meltspun process.

Companies involved in selling machines or providing nanofiber-based solutions using electrospinning technology include Elmarco, Finetex, eSpin Technologies, Donaldson, Dienes Apparatebau GmbH, SNS Nanofiber Technology, Ahlstrom, and TopTec.

Read full chapter

URL: https://www.sciencedirect.com/science/article/pii/B9780080983011000046

Cake filtration with a composite micro–nanofiber filter

Wallace Woon-Fong Leung ScD (MIT), in Nanofiber Filter Technologies for Filtration of Submicron Aerosols and Nanoaerosols, 2022

7.7 Cake deposition pattern

7.7.1 Nanofiber filter

For a nanofiber filter, once cake starts to deposit on the filter surface, the cake properties, namely, the porosity and permeability, can be determined. A rather impermeable cake results from the two nanofiber filters with fiber diameters 187 and 283 nm with low permeability $2.57(10^{-13})$ and $2.73(10^{-13})$ m^2, respectively. The cake can be perceived as shown in Fig. 7.14A. (This schematic perception is supported by CFD simulation in Chapter 9: Numerical Modeling of Aerosol Filtration Using a Nanofiber Filter.) With a composite nanofiber–nanofiber filter with tighter flowable pore size, the permeability of, $2.44(10^{-13})$ m^2 is not much better.

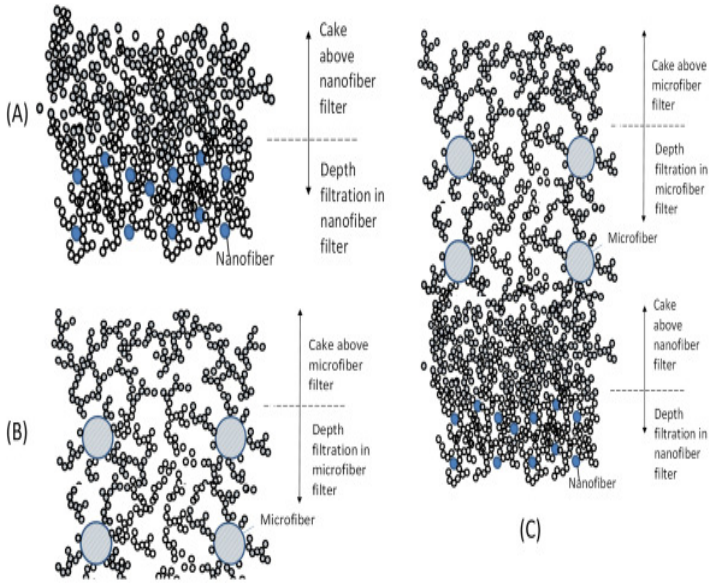

Figure 7.14. (A) Nanofiber filter has trapped aerosols in the filter and in the cake layer formed. Aerosols are densely and randomly packed around nanofibers and above the cake layer that is quite impermeable; (B) microfiber filter has trapped aerosols in the filter and in the cake layer formed above the filter. Dendritic structures formed around the larger surface of the microfiber filter help to space out the deposited aerosols; (C) nanofiber layer is packed with aerosols. Microfiber layer above the nanofiber layer filter has trapped aerosols but dendritic structures formed around the larger surface of the microfiber layer space out the aerosols rendering a more porous packing. There are two cake fronts competing in growth: one that initiates from the microfiber layer and another from the underlying nanofiber layer. The cake front from the microfiber layer grows at a faster rate to form a porous cake layer cutting off incoming aerosols from further depositing downstream on the impermeable cake layer of the nanofiber layer.

7.7.2 Microfiber filter

On the other hand, a more porous microfiber filter with a mean fiber diameter of 2.7 μm yields a cake permeability of $4.50(10^{-13})$ m^2, which nearly doubles that of the nanofiber filter. This is represented schematically by Fig. 7.14B (supported by CFD in Chapter 9: Numerical Modeling of Aerosol Filtration Using a Nanofiber Filter).

7.7.3 Microfiber–nanofiber composite filter

An intriguing issue is when a microfiber is placed upstream of the nanofiber filter to form a composite filter, from separate CFD results, two cake layers would form, respectively, on the surface of the microfiber layer as well as at the interface of the microfiber layer–nanofiber layer (growing into the upstream microfiber layer with continuous aerosol deposition), both attributed to the “skin effect” from each layer (Leung & Choy, 2018a; Leung & Hung, 2012). The cake from the nanofiber would be rearranged as the cake grows passed by the microfibers in the microfiber layer. When the cake from the nanofiber grows into the upstream microfiber layer, the cake would have a permeability better than that of a single nanofiber layer alone as the cake would be “restructured and reorganized” by both the dendrites/dendritic structure deposited on the microfibers and the microfibers themselves. On the other hand, the cake originating from the skin layer of the microfiber also grows as well, and if it grows sufficiently fast, it can grow above the surface of the microfiber layer capturing all incoming aerosols and cutting off further aerosols escaping downstream to the nanofiber layer. Which scenario would ultimately take control? The answer can be found from the outcome of the test, i.e. the cake in the composite filter, which can be identified by its permeability. From the experimental results, we found that indeed the permeability of the cake on the microfiber–nanofiber composite $5.87(10^{-13})$ m^2 is closely related to that of the microfiber filter $4.50(10^{-13})$ m^2 and not related to that of the 187-nm diameter nanofiber filter of

$2.57(10^{-13})$ m^2. Thus it is concluded that the cake forms on the microfiber layer outpaces that from the nanofiber layer downstream, which is extremely advantageous! A rationale is that the microfiber layer is located upstream and, therefore, receives and captures the incoming aerosols especially when a preliminary cake layer has formed on its surface. Any uncaptured aerosol by the microfiber layer escapes downstream to the nanofiber layer which has much lower aerosol concentration; therefore the likelihood of the cake from the nanofiber outpacing that of the microfiber layer is very slim unless the upstream microfiber layer has a very poor filtration efficiency (see such a scenario in Chapter 9: Numerical Modeling of Aerosol Filtration Using a Nanofiber Filter). In other words, the microfiber–nanofiber composite filter yields a cake that is almost the same or better than the single microfiber filter. This is represented schematically by Fig. 7.14C (supported by CFD in Chapter 9: Numerical Modeling of Aerosol Filtration Using a Nanofiber Filter), which is quite remarkable.

Flow of Fluids Through Granular Beds and Packed Columns

In Coulson and Richardson's Chemical Engineering (Sixth Edition), 2019

7.7 Pressure Drop in Fibrous Porous Systems

Undoubtedly, most porous media and packed columns are made up of granular particles; there are, however, similar systems composed of long particles, fibres, etc., and are characterised by high values of voidage, as large as $e = 0.98–0.99$. The flow of fluids in such media is encountered in a broad spectrum of applications, including aerosol filtration, production and processing of fibre-reinforced polymer and metal composites, drying of fibrous foodstuffs, cotton batting, textile fibres, biomedical settings, etc. In such cases, additional advantages accrue on account of their high porosity (and hence, large specific surface area), relatively low resistance to flow, high rates of mass and heat transfer, etc. Consequently, over the years, a reasonable body of knowledge has accrued which has been reviewed by Jackson and James,[71] Chen et al.,[72] Johnson and Deen,[73] Mattern and Deen,[74] etc.; the latter two references focus on aerosol gels, ligaments and tendons, etc.

In the streamline flow regime, Jackson and James[71] have collated much of the literature data and represented it in the form of dimensionless permeability, B/r^2, defined by Eq. (7.1), r being the radius of the fibre. They correlated (B/r^2) with the mean voidage of the system. Notwithstanding considerable scatter of data, especially at small values of e, they put forward the following empirical correlation for $e > \sim 0.6$:

$$\left(B/r^2\right) = -10.68 + 39.33e - 58.75e^2 + 32.05e^3 \tag{7.58}$$

The available experimental results suggest the Kozney constant K'' to lie in the range of 4 to 5 for these systems also. Detailed discussion on this topic in the context of the flow of both the Newtonian and non-Newtonian fluids in such porous media is available in Ref. 27. Suffice it to add here that the flow resistance is influenced by the wettability of the fibres, their stiffness and cross-section, orientation, etc., in addition to the overall voidage and the flow conditions.

MACROSCOPIC DESCRIPTION OF FIXED-BED GRANULAR FILTRATION

Chi Tien, B.V. Ramarao, in Granular Filtration of Aerosols and Hydrosols (Second Edition), 2007

2.5.2 Determination of the Function $F(\alpha, \sigma)$

As discussed before, $F(\alpha, \sigma)$ describes the effect of deposition on the filtration rate. Since at a given axial distance, the particle concentration in the fluid, c, reflects the extent of filtration occurring in the filters up to that distance, the data for c versus z obtained at different times, together with knowing the value of λ_0, provide the basis for determining the function, F.

Determining F from experimental filtration data is a two-step process. First, one must select a specific functional form of F, containing a number of undetermined constants. Second, function F's undetermined constants (represented by the components of the parameter vector α) are determined by requiring that predicted and experimental values closely agree. There exists no fixed, specific procedure for selecting the expression for $F(\alpha, \sigma)$ although some guidelines are available. As discussed under Section 2.2.1, the effect of deposition on the filtration rate can be classified into three types: favorable, unfavorable, or a combination of both (namely, first favorable then unfavorable, or vice versa). One can identify the particular type of behavior exhibited by inspecting the experimental data of c versus z collected at various times. The following observations may prove useful.

(a) If the particle concentration profile c versus z, does not vary with time, or

$$\left(\frac{\partial c}{\partial \theta}\right)_z = 0,$$

it implies that the filtration rate does not exhibit any change during the course of filtration. Accordingly,

$$F\left(\underline{\alpha}, \sigma\right) = 1$$

(b) If the concentration profiles, c versus z, obtained at different times show a systematic displacement – in particular, if the profiles are displaced downward as θ increases, or $\left(\frac{\partial c}{\partial \theta}\right)$ is always negative – it means that the rate of filtration in the filter is enhanced as the filter becomes progressively clogged. A simple expression of F would be

$$F = 1 + b\sigma$$

or

$$F = 1 + b\sigma^2$$

Conversely, if the concentration profiles, c versus z, at different times are displaced upward as θ increases, or $\left(\frac{\partial c}{\partial \theta}\right)$ is always positive, then the behavior suggests that the rate of filtration decreases as increases. Consequently, one may consider F to be of the form

$$F = 1 - b\sigma$$

or

$$F = 1 - b\sigma^2$$

The former behavior is almost always seen in aerosol filtration. For hydrosol filtration, the so-called filter-ripening phenomenon refers to the situation in which the rate of filtration increases with the extent of deposition (increase in σ). On the other hand, if deposition leads principally to the clogging of the pores of the filter media, then one often also observes a deterioration in effluent quality with time.

(c) The mixed behavior can be detected either of two ways: It may be evident from the behavior of the concentration profiles c versus z at various times. The mixed behavior may also be noticeable when a least-squares fit is performed on the

concentration profile data obtained at a given time. This operation may point up a trend in the discrepancies between the parameter values for one of the expressions previously mentioned.

For a filter to exhibit the mixed behavior, *F* must display similar behavior; in other words, if the filter performance first improves with time then deteriorates with time, then *F* must first increase with σ, reaching a maximum, and then decrease. The last three expressions of *F* listed in Table 2.1 are capable of describing this mixed behavior.

(d) The presence of the detachment of deposited particles can be seen if $c| > c|_{z_1}$ at any instant (constant θ) for $z_2 > z_1$ since without detachment, suspension particle concentration is a monotonically nonincreasing function of filter depth.

A number of procedures for the determination of *F* have been developed in the past. A brief discussion of some of these parameters is given below.

2.5.2.1 Procedures based on uniform deposition assumption

If one assumes that particle deposition with a filter depth *L* is uniform, the average specific deposit at any time (θ), $\bar{\sigma}$, can be determined for overall mass balance consideration, or

$$\bar{\sigma} = \frac{1}{L}\int_0^L u_s\,(c_{in} - c_{eff})\,dz \tag{2.60}$$

$\bar{\lambda}$

The corresponding average filter coefficient, , is given

$$\bar{\lambda} = \frac{1}{L}\ln\,(c_{in}/c_{eff}) \tag{2.61}$$

from which the values of $\bar{\lambda}/\lambda_0$ can be obtained and the relationship of λ/λ_0 versus σ established.

The uniform deposition assumption becomes more valid and the filter bed decreases. Based on this argument, Walata et al. (1986), in their aerosol studies, proposed a limiting procedure in order to obtain accurate expressions of *F*. From their experimental data, it was found that $\bar{\lambda}/\lambda_0$, in many cases, can be related to $\bar{\sigma}$ by the power-law expression

$$\frac{\bar{\lambda}}{\lambda_0} = 1 + \bar{\alpha}_1\bar{\sigma}^{\bar{\alpha}_2} \tag{2.62}$$

By evaluating $\bar{\alpha}_1$ and $\bar{\alpha}_2$ from data obtained using filters of different depth and then by extrapolating $\bar{\alpha}_1$ (and $\bar{\alpha}_2$) against filter depth, the respective limiting values of α_1 and a_2 as $L \to 0$ can be determined, which were taken from those of the correct expression of *F*. A more detailed discussion of Walata et al.'s procedure is given in Chapter 6.

2.5.2.2 Determination of *F* according to Eqn (2.56)

The effluent concentration for the case of *F* being a linear function of σ is given by Eqn (2.56) which may be rearranged to give

$$\frac{(c_{in}/c_{eff})-1}{[\exp(\lambda_0 L)]-1} = \exp\,[-u_s\lambda_0 c_{in} k\theta] \tag{2.63}$$

In other words, a plot of $(c_{in}/c_{eff}) - 1$ against θ on a seminatural logarithmic scale yields a straight line with an intercept of $[\exp(\lambda_0 L)] = 1$ and a slope of $-u_s\lambda_0 c_{in} k$. The effluent concentration history together with Eqn (2.63) can then be used to obtain the values of λ_0 and *k* (therefore *F*). On the other hand, if such a linearity is not observed, one may surmise that *F* is not given by $1 - k\sigma$. As an approximation, one may take the slope of the tangent to the curve of $\ln[(c_{in}/c_{eff}) 1]$ versus σ as the instantaneous value of $-u_s\lambda_0 c_{in} k$ corresponding to the average σ according to Eqn (2.60) thus establishing a relationship between *k* and σ (or *F*).[2]

2.5.2.3 Determination of *F* as a search-optimization problem

Determination of F from experimental data can be treated as a problem of search and optimization. First a particular expression of F is chosen based on the general consideration stated before, and search and optimization procedure can then be used to obtain the values of the constants present in F. The procedure required has the following elements.

(a) A method for integrating the macroscopic equations of granular filtration with the assumed expressions for $F(\alpha, \sigma)$ and the values of the constants to yield concentration profiles at various times;

(b) A search-optimization technique to determine the values of the constants of $F(\alpha, \sigma)$ in order to obtain the best agreement between predictions and experiments; and

(c) An initial estimate of the parameters of F.

The method of Herzig et al. (1970) discussed in Section 2.4 can be used for (a). A variety of techniques are available for the determination of the parameters present in F. Payatakes et al. (1975) applied the Levenberg modification of the Gauss–Legendre algorithm in treating the filtration data of clay suspensions. Assume that the experimental data of particle concentration profiles, c versus z at various times, are available. Let c_{km}, denote the value of c at $z = z_m$ and $\theta = \theta_k$, $m = 1, 2, \ldots M$ and $k = 1, 2, \ldots K$. The search for the parameter vector α appearing in $F(\alpha, \sigma)$ [or $N(\alpha, c, \sigma)$ for the more general case], with the components of α corresponding to the undetermined parameters present in the assumed expression of F (or N), is based on minimizing the objective function, $\psi(\alpha)$, defined as

$$\psi\left(\underline{\alpha}\right) = \sum_{k=1}^{K} \sum_{m=1}^{M} \left[c_{km} - c\left(z_m, \theta_k, \underline{\alpha}\right)\right]^2 \tag{2.64}$$

The quantity within the bracket of the above expression is the difference between the experimental concentration value and the predicted value based on the assumed F_1. Under the double summation signs of Eqn (2.64) there are $R = K \times M$ such differences which form a column vector, φ as

$$\underline{\varphi} = \begin{bmatrix} \varphi_1 \\ \varphi_2 \\ \cdot \\ \cdot \\ \cdot \\ \cdot \\ \cdot \\ \varphi_R \end{bmatrix} = \begin{bmatrix} c_{11} - c(z_1, \theta_1, \underline{\alpha}) \\ \cdot \\ \cdot \\ c_{1M} - c(z_M, \theta_1, \underline{\alpha}) \\ \cdot \\ \cdot \\ c_{K1} - c(z_1, \theta_K, \underline{\alpha}) \\ \cdot \\ \cdot \\ c_{KM} - c(z_M, \theta_K, \alpha) \end{bmatrix} \tag{2.65}$$

In obtaining the optimum value of α, α_{opt} which gives a minimum value of $\psi(\alpha)_i$ for a given α, one can better approximate α_{opt} with $\alpha + \Delta\alpha$. According to Levenberg (1944), the correcting term, $\Delta\alpha$, for a strongly nonlinear system (such as the equations describing the dynamic behavior of aerosol and hydrosol granular filtration), is

$$\Delta\underline{\alpha} = -\left(\underline{\underline{J}}\,\underline{\underline{J}}^{\mathrm{T}} - \chi\underline{\underline{I}}\right)\underline{\underline{J}}\underline{\varphi} \tag{2.66}$$

where $\underline{\underline{I}}$ is a unit $N \times N$ matrix. $\underline{\underline{J}}$, the Jacobian (and $\underline{\underline{J}}^{\mathrm{T}}$ the transpose of $\underline{\underline{J}}$), is given as

$$\underline{\underline{J}} = \begin{bmatrix} \frac{\partial \varphi_1}{\partial \alpha_1} & \cdots & \frac{\partial \varphi_R}{\partial \alpha_1} \\ \vdots & & \vdots \\ \frac{\partial \varphi_1}{\partial \alpha_N} & \cdots & \frac{\partial \varphi_R}{\partial \alpha_N} \end{bmatrix} \tag{2.67}$$

The quantity χ is known as the Levenberg parameter. Payatakes et al. (1975) suggested that

$$\chi = -\frac{\left|\underline{\underline{J}}\varphi\right|}{r} \tag{2.68}$$

and

$$r = \frac{1}{20}\left|\left(\underline{\underline{J}}\,\underline{\underline{J}}^{\mathrm{T}}\right)^{-1}\underline{\underline{J}}\varphi\right| \tag{2.69}$$

The search-optimization procedure, was proved efficient, and convergence to the optimum usually not sensitive to the initial estimate of α used. An example of the optimization search is given below.

Example of the integral parameter search method

The following example is taken from Payatakes et al. (1975).

Filter bed: granular activated carbon “DARCO” 20 × 40

Mean geometric grain diameter = 0.594 mm

Filter bed ID = 76 mm

Depth of filter = 1.3 m

Macroscopic porosity, $\varepsilon_0 = 0.49$

Suspension:

Clay (EPK) in Syracuse tap water

Suspended particle size: nonuniform 4 μm < d_p < 40 μm

Influent concentration: c_{in} = 88 vol. ppm (218 wt ppm)

Superficial velocity: u_s = 4.96 m/h (1.38 mm/s)

F and *G* are assumed to be:

$$F = \frac{1}{(1+\alpha_1\sigma)^2}$$
$$G = 1 + \beta_1$$

Using the parameter estimation method described above based on the data shown in Figs 2.6 and 2.7 yields

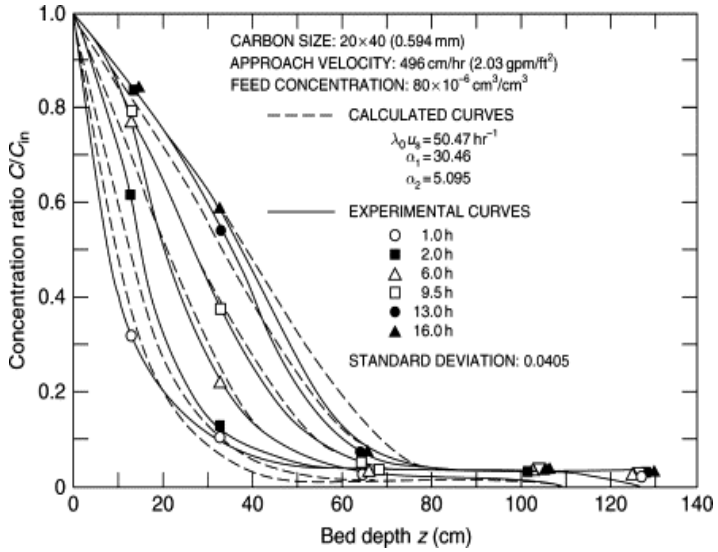

Fig. 2.6. Suspension particle concentration distribution for filtration through 20 × 20 carbon bed (Mehter et al., 1970).

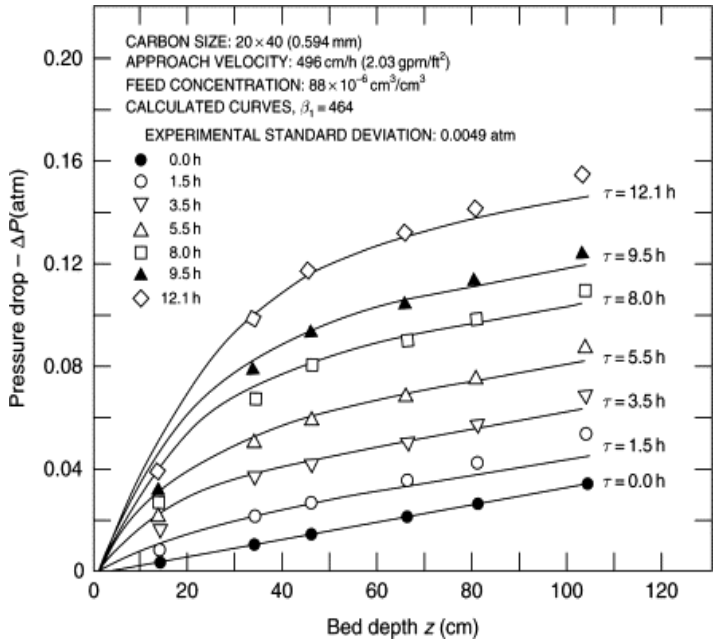

Fig. 2.7. Headloss for filtration through 20 × 20 carbon bed (Mehter et al., 1970).

$$\lambda_0 = 1.02 \times 10^{-2}\,\mathrm{mm}^{-1}$$
$$\alpha_1 = 30.46 \qquad \alpha_2 = 5.095$$
$$\left(\frac{dp}{dz}\right)_{\sigma=0} = 3.36 \times 10^{-2}\,\mathrm{atm\,m}^{-1},\ \beta_1 = 464$$

Calculated c/c_{in} versus z curves and ΔP versus z curves at various times θ_k are also plotted in Figs 2.6 and 2.7, respectively. As can be seen, the phenomenological equations are quite effective in describing the filtration system.

A simpler procedure for the determination of F was developed recently by Bai and Tien (2000b) assuming that F is a polynomial σ. A detailed discussion of the Bai–Tien procedure in the determination of F from data displaying different behavior is given in the Supplement of this volume.

COLLECTOR EFFICIENCY OF AEROSOLS IN GRANULAR MEDIA

Chi Tien, B.V. Ramarao, in Granular Filtration of Aerosols and Hydrosols (Second Edition), 2007

6.3 EXPERIMENTAL DETERMINATION OF INITIAL COLLECTOR EFFICIENCY

6.3.1 Apparatus for Experimental Measurement

Although there is no standard equipment for determining the initial collector efficiency, various investigators have used rather similar apparatuses.

Generally, the experimental apparatus used to determine aerosol collector efficiency consists of three major components: a test filter, an aerosol generating system, and instruments for determining aerosol concentration. Preparing an experimental filter does not present any significant difficulty, although it should be mentioned that uniform packing is not always assured especially if the filter is short. The ratio of the filter diameter to the filter-grain size should be large enough that the nonuniform porosity near the filter wall will have no significant effect on the results. A schematic diagram of the apparatus used by Thambimuthu (1980) is shown in Fig. 6.11 as an example.

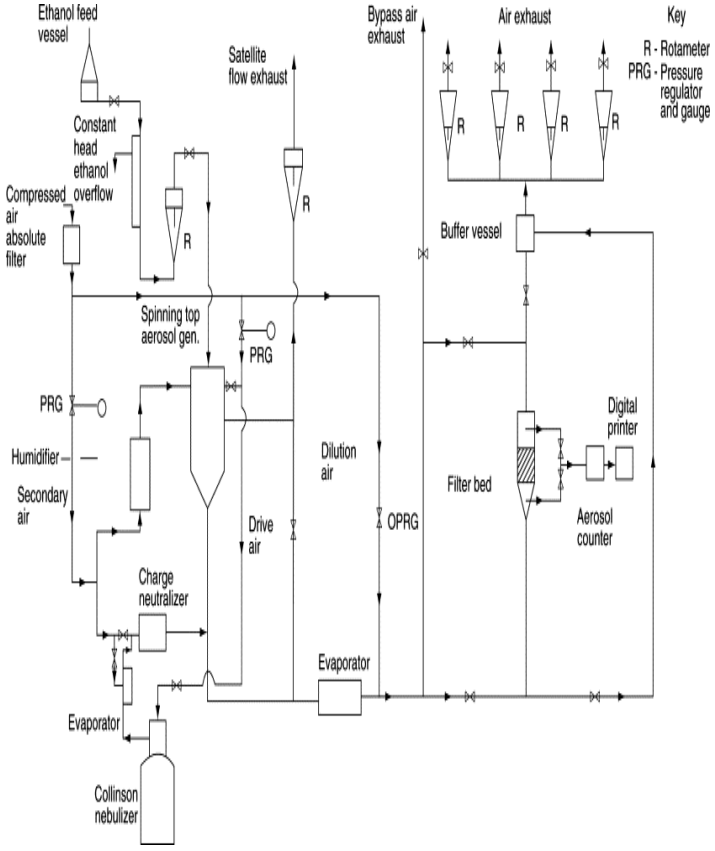

Fig. 6.11. Experimental apparatus for determining η_0 used by Thambimuthu (1980).

Particle concentration can be measured with particle counters, a variety of which, based on different principles according to particle size are available commercially. Depending on its concentration, the sample to be tested may require dilution. Similarly, a variety of devises can be used for generating test aerosols (either in liquid or solid forms), including the condensation generator, rotating-disk generator, and the vibrating capillary generator. Test aerosols can also be prepared

by nebulizing liquid suspensions of certain types of particles of specific size (for example, latex particles). After nebulization, the liquid is removed by drying to produce solid-particle aerosols. This procedure has been a common practice for the study of aerosol filtration in granular media.

6.3.2 Concentration Measurement Accuracy and Its Effect on η_0

Regardless of the specific apparatus used, the purpose of the experimental work is to yield the values of C_{in}/C_{eff} from which the initial collector efficiency, η_0, can be calculated by applying Eqn (6.15). As η_0 is proportional to the logarithm of the concentration ratio, C_{in}/C_{eff}, the accuracy one may expect in determining η_0 depends on the accuracy of the particle concentration measurements as well as the extent of removal the experiment achieves.

To illustrate this point, Table 6.2 shows an error propagation in the calculation of η_0 from values of influent and effluent concentrations. The uncertainties involved in determining η_0 from Eqn (6.15) are calculated for various values of C_{eff}/C_{in} and the instrument accuracy in determining C_{in} and C_{eff}, which is given in terms of the accuracy relative to C_{in}. For example, consider the first entry on Table 6.2 and assume that the values of C_{in} and C_{eff} (in number of particles/cm^3) are 100 and 80, respectively. If the accuracy of the concentration value is ±1% (or one particle), then the measured values of C_{in} and C_{eff} may vary from 99 to 101 particles and from 79 to 81, respectively. These measured values, in turn, give a value of C_{eff}/C_{in}, ranging from a minimum of 79/101 = 0.782 to a maximum of 81/99 = 0.818. The corresponding logarithms for C_{in}/C_{eff} are 0.201 and 0.246, respectively, while the correct value should be ln(100/80) = 0.223. The minimum and maximum values of η_0 (in reference to the correct value) are 0.90 and 1.10. In other words, we may expect a 20% difference.

Table 6.2. Error propogation in calculation of experimental collection efficiency error in concentration measurement, relative to feed concentration

		±1%			**±5%**			**±10%**	
C_{in}		100			100			100	
C_{in}^{+}		101			105			110	
C_{in}^{-}		99			95			90	
C_{eff}	80	50	20	80	50	20	80	50	20
C_{eff}^{+}	81	51	21	85	55	25	90	60	30
C_{eff}^{-}	79	49	19	75	45	15	70	40	10
C_{eff}/C_{in}	0.800	0.500	0.200	0.800	0.500	0.200	0.800	0.500	0.200
$(C_{eff}/C_{in})^{+}$	0.818	0.515	0.212	0.895	0.579	0.263	1.00	0.667	0.333
$(C_{eff}/C_{in})^{-}$	0.782	0.485	0.188	0.714	0.429	0.143	0.636	0.364	0.091
$-\ln(C_{eff}/C_{in})$	0.223	0.693	1.609	0.223	0.693	1.609	0.223	0.693	1.609
$[-\ln(C_{eff}/C_{in})]^{+}$	0.246	0.724	1.671	0.337	0.846	1.945	0.000	0.405	1.100
$[-\ln(C_{eff}/C_{in})]^{-}$	0.201	0.664	1.551	0.111	0.546	1.336	0.453	1.011	2.397
$\left(\lambda_0^{+}/\lambda_0\right)$ or $\left(\eta_0^{+}/\eta_0\right)$	1.10	1.04	1.04	1.51	1.22	1.21	2.03	1.45	1.50
$\left(\lambda_0^{-}/\lambda_0\right)$ or $\left(\eta^{-}/\eta_0\right)$	0.9	0.96	0.96	0.50	0.79	0.83	0.00	0.58	0.68

Superscripts^{+} and^{-} denote the upper and lower limits of uncertainty, respectively.

The results shown in Table 6.2 lead to some interesting conclusions. One is that a relatively small error (e.g., 1%) in concentration measurement at a removal level of 20% (namely, $C_{eff}/C_{in} = 0.8$) may lead to a 20% uncertainty in determining η_0. The results also suggest that for a given instrument accuracy, there is an optimum removal level at which the experiment should be conducted.

The accuracy of experimentally determined collector efficiency and the effect of the particle counter used were assessed by Walata (1985) and Jung et al. (1989). The assessment was made by examining the consistency and reproducibility of the η_0 values obtained. The particle counter effect was also examined by comparing results obtained from using different particle counters. As an example of demonstrating data internal consistency, Fig. 6.12 shows the influent and effluent concentrations of three experimental runs carried out under essentially the same conditions ($d_p = 2.02$ μm, $d_g = 505$ μm, $u_s = 5.55$ cm/s, $L = 0.696 \pm 0.04$ cm) except the influent concentration (two of which were nearly the same approximately 40 particles/cm^3 while that one at approximately twice the value) over a period of nearly 60 min. The variations of c_{in} versus time showed the capability of the nebulizer used in generating test aerosols on a consistent and steady basis. The influent/effluent concentration ratio versus time given in Fig. 6.12 indicates that the concentration ratio C_{eff}/C_{in} remained essentially the same and that there was no effect due to the influent concentration. That there was no time-dependence of η_0 indicated that the extent of deposition throughout the experimental filter was slight and throughout the period of experiments the filter bed can be assumed to be in its initial state.

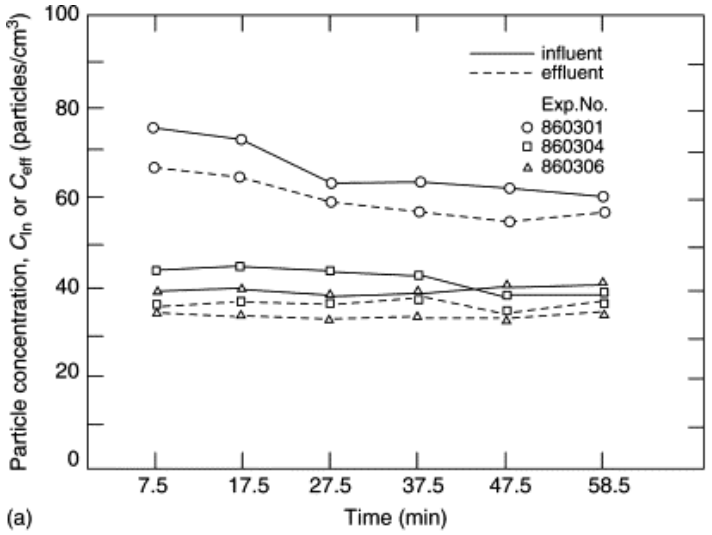

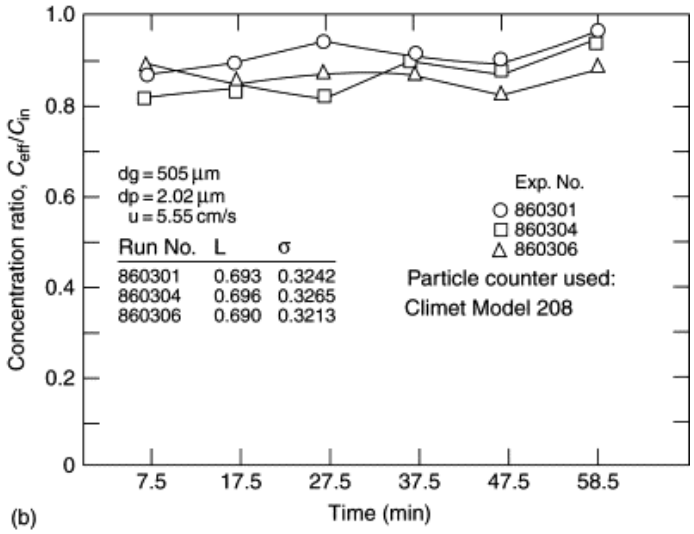

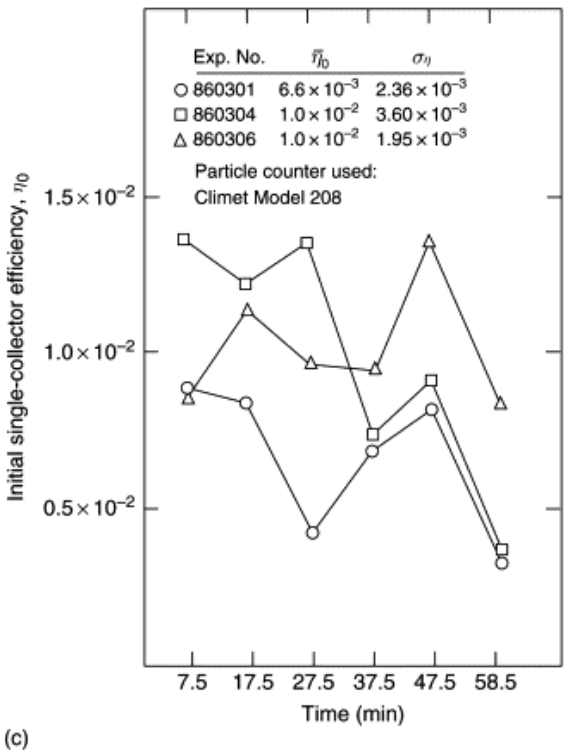

Fig. 6.12. Experimental determination of η_{s_0} (a) influent/effluent concentration histories, (b) concentration ratio versus time, (c) η_{s_0} versus time.

The initial single-collector efficiency calculated according to Eqns (6.15) and (6.16c) versus time is shown in Fig. 6.12. The scattering of results was significantly greater than what was shown in Fig. 6.12. This difference is, of course, a direct consequence of the logarithmic relationship between the concentration ratio and the collector efficiency of Eqn (6.15). The same kind of behavior was also found in all other cases using different types of particle counters.

A simple statistical analysis of the data obtained by Jung et al. (1989) provided some useful information about the experimental accuracy in the determination of η_0. Table 6.3 gives the average $\bar{\eta}$ value of six experimental runs carried out under identical operating conditions (except influent concentration). The average collector efficiency $(\eta_0)_{av}$ of each run was based on six data points taken over a period of approximately 1 h. Also included in the table are the standard deviations, $\sigma_{(\eta_0)_{av}}$. In all cases, the ratio of $\sigma_{(\eta_0)_{av}}/(\eta_0)_{av}$ is less than 0.36.

Table 6.3. Internal consistency of experimentally determined η_0 (Jung et al., 1989)

Run No.	Average value of η_0, $\bar{\eta}_0$	Standard Deviation of η_0, $\sigma_{\bar{\eta}_0}$	$\sigma_{\bar{\eta}_0}/\bar{\eta}_0$
86 301[a]	6.6×10^{-3}	2.36×10^{-3}	0.358
86 304[a]	1.0×10^{-2}	3.6×10^{-3}	0.360
86 306[a]	1.0×10^{-2}	1.95×10^{-3}	0.195
86 302[b]	6.17×10^{-3}	2.22×10^{-3}	0.36
86 303[b]	1.06×10^{-2}	1.98×10^{-3}	0.18
86 305[b]	7.7×10^{-3}	2.47×10^{-4}	0.11

Based on six data points collected over a period of approximately 1 h. The experimental conditions were d_p = 2.02 μm, d_g = 508 μm, L = 0.69 cm, ε = 0.32–0.33, and u_s = 5.5 cm/s.

a Climet counter used for concentration measurement.

b H/R counter used for concentration measurement.

Read full chapter

URL: https://www.sciencedirect.com/science/article/pii/B9781856174589500075

Electret filter for depth and cake filtration

Wallace Woon-Fong Leung ScD (MIT), in Nanofiber Filter Technologies for Filtration of Submicron Aerosols and Nanoaerosols, 2022

8.11.2 Loading capacity and pressure drop

It is desirable for a filter to have large aerosol storage capacity but with low incurred pressure drop. The typical pressure drop versus loading for a filter is depicted schematically in Fig. 8.24B.

With reference to Fig. 8.24B, starting from a clean filter with initial pressure drop Δp_m attributed to resistance to air flow from the fibers in the clean filter, there are two regimes of operation: depth filtration followed by cake or surface filtration. During depth filtration, aerosols are trapped and deposited in the filter until it reaches Point 1 in the figure, where the filter efficiency of all challenging aerosols

(i.e., all sizes, note the large aerosols can reach 100% faster than the small aerosols) reaches 100%, the total specific mass deposit M_s reaches ΔM_D, and the pressure drop has increased to Δp_1. It is to be noted that Point 1 in Fig. 8.24B marks the ending of depth filtration and the beginning of surface/cake filtration, where the challenging aerosols are captured and forms a cake on the filter surface. The cake becomes the effective filter medium and its thickness continues to increase with more aerosol deposition on the cake surface. The pressure drop, Δp, continues to build up and eventually a "structured cake" forms on the filter surface with approximately constant permeability or specific cake resistance, which can be determined from the slope of the linear segment of the Δp escalation curve. This has been discussed extensively in Chapter 6, Transition from Depth-to-Surface Filtration for a Nanofiber Filter. Once the pressure drop of the entire filter reaches an arbitrary set maximum pressure drop, Δp_2 (Point 2 in Fig. 8.24B), filtration ends and the loaded filter needs to be replaced or regenerated see Chapter 10, Cleaning Nanofiber Filter. For the entire filtration process, there are some interesting issues:

Which filter among the four filters considered has the maximum aerosol deposit at the end of the filtration when the pressure drop reaching Δp_2?

For each filter, how much aerosols are being deposited during depth and cake filtration, respectively?

What is the pressure drop, respectively, in depth and cake filtration?

What is rate of change of pressure drop with additional specific mass deposit during cake buildup?

Table 8.1 summarizes the essential answers to the questions for the four filters—SU, MU, SC, and MC. Obviously, given the total pressure drop due to loading is given by $\Delta p_2 - \Delta p_m$, it is desirable to reduce pressure rise gradient in both depth filtration $(\Delta p_1 - \Delta p_m)/\Delta M_D$ and in cake filtration $(\Delta p_2 - \Delta p_1)/\Delta M_C (= \Delta p_C/\Delta M_C)$, respectively. Both rate of change in pressure drop per unit change in aerosol deposit are determined for the four filters in Table 8.1. (Note: The slope of the tangent to the pressure drop excursion curve in the cake regime for a given filter can be determined from Fig. 8.24A and it is also reported in Table 8.1 under "slope". The slope is comparable in magnitude to $\Delta p_C/\Delta M_C$.) Unfortunately, a small rate of change in pressure drop per unit aerosol deposit in depth filtration leads to a much larger rate of change in cake filtration, and vice versa, but not both. To aim for high filter capacity, the goal is to maximize the total specific mass deposit in the filter in both depth filtration, ΔM_D, as well as cake filtration, ΔM_C. This will be apparent in the following.

Table 8.1. Pressure drop and deposit mass during depth and cake filtration.

	Depth filtration					Ca		
Filter	**Media Δp**	**(1) End of depth filtration (i.e., 100% efficiency)**				**(2) End of c**		
	Δp_m (Pa)	ΔM_D (g/m^2)	Δp_1 (Pa)	$(\Delta p_1 - \Delta p_m)/\Delta M_D$ [Pa/(g·m^{-2})]	Δt (h)	Slope [Pa/(g·m^{-2})]	$\Delta M_D + \Delta M_C$ (g/m^2)	ΔM_C (g/m^2)
SU	20.8	6.5	181	25	4	40	24	17.5
SC	21.1	6.8	168	22	3	35	26.4	19.6
MU	16.9	16.8	337	19	14	53	26.4	9.64
MC	18.1	26.1	316	11	12	49	36.5	10.4

Read full chapter

Numerical modeling of aerosol filtration using a nanofiber filter

Wallace Woon-Fong Leung ScD (MIT), in Nanofiber Filter Technologies for Filtration of Submicron Aerosols and Nanoaerosols, 2022

9.1.1 Literature on aerosol loading

We have seen that the aerosol loading process for fibrous filters generally proceeds through three regimes: (1) initial depth filtration regime, (2) transition filtration regime, and (3) cake filtration regime (Japuntich et al., 1997). These three regimes for monodispersed aerosol filtration have been identified experimentally earlier (Japuntich et al., 1994). In the first regime, aerosols deposit within the filter and the pressure drop slightly increases with mass loading. In the second regime the captured aerosols start collecting incoming aerosols and clogging commences increasing further the pressure drop. In the third regime the filter cake is formed and the pressure drop increases rapidly. These three regimes of filtration have not been studied systematically, especially the transition regime, see Chapter 6, Transition from Depth-to-Surface Filtration for a Nanofiber Filter. At present, many studies only consider one or two of them, and mostly on cake filtration. The dendrite structures that form on the fiber surface were modeled by Payatakes et al. (Payatakes, 1977); however, these models are limited due to neglecting the effects of the dendrite upon the flow field. Hosseini and Tafreshi (2012) developed a methodology for simulating pressure drop and collection efficiency of a filter medium during instantaneous aerosol loading using the ANSYS–Fluent CFD code. They have enhanced the code with in-house subroutines. Schmidt (Schmidt & Löffler, 1991) observed that the porosity of dust cake layer decreased with increasing pressure drop and, therefore, proposed a simulation program based on a simple model, by which local transient porosities inside the dust cake and the pressure drop as a function of time can be calculated. Silva et al. (1999) proposed a model incorporating an increase in the superficial velocity of filtration as a result of decreasing cake porosity and increasing cake-specific resistance. Thomas et al. (2001) described the effect of deposited aerosols as two stages. During the first stage, with a small increase of pressure drop, the filter efficiency grew dramatically until reaching the loading point of cake formation. However, during the second stage, the rate of efficiency increase was being slowed down. Further, Thomas et al. (2014) presented a new pressure-drop model developed for cakes composed of nanostructured aerosols with (i.e., aggregates) or without partial overlapping of aerosols. However, these models required an assumption of the deposit geometry or the onset of cake formation, and the aerosol sizes were monodispersed. As known, aerosols are polydispersed instead and monodispersed size distribution is only an idealized model used in exploratory simulation to get some basic understanding prior to launching the more complicated polydispersed aerosol size distribution. It is worth noting that not only the total amounts of deposited aerosols but also their spatial distribution of these polydispersed aerosols and resulting cake structure affect filter performance (Przekop & Gradoń, 2008). Therefore the study on the filtration process of polydispersed aerosols (encompassing all three regimes – depth filtration, transition, and cake filtration) has both practical and theoretical significance.

Studies of the filtration of polydispersed aerosols are rather scarce. Endo et al. (1998) presented a new analytical equation of dust cake, including the effects of polydispersity and shape factor of the aerosols, which had significant effect on filter loading. However, the complicated equation and insufficient accurate coefficient limited their applications. Kim et al. (2000) studied the diffusion filtration of polydispersed aerosols using a numerical method. An analytical solution was derived for the change in aerosol size distribution (Kwon et al., 2002). This solution, however, was valid only for small aerosols because inertial impaction was not accounted for. Rosner et al. (1995) verified that the local size distribution of aerosols deposited by inertial impaction on a cylindrical target has retained log-

normal shape provided that the mainstream aerosol suspension was also log-normal. Baumgartner and Löffler (1987) demonstrated the three-dimensional (3D) structures of deposited polydispersed aerosols obtained from their numerical simulations; however, only a qualitative picture of deposits was presented. Maze et al. (2007) simulated the cake formation process in 3D nanofibrous filter media at reduced pressure drop for different monodispersed and polydispersed aerosols.

Despite these efforts, a lot of issues remain unanswered. In this chapter, we want to use numerical modeling to study the depth filtration, transition, and cake filtration. In particular, we want to study the maldistribution of aerosol deposition in a filter leading to the formation of skin layer. Prior to the formation of the skin layer, how do dendrites or dendritic fibers form from the aerosol deposition? How do these dendritic structures interact with each other? How can the skin layer get clogged by these aerosol depositions and dendritic structures to a point at which aerosol deposit starts emerging above the filter (i.e., from depth- to surface-filtration)? How does the cake form on the filter surface? For the abovementioned issues, what is the difference between monodispersed versus polydispersed aerosol size distribution challenging the filter from depth to cake filtration? When a cake forms, do incoming aerosols deposit uniformly on the existing cake surface forming a stratified or layered structure, and do smaller aerosols stay on the cake surface or penetrate into the cake layer formed by the larger deposited aerosols? These questions are quite intriguing and complicated, yet they are important for our understanding and are complementary to what has been discussed in Chapter 6 - Transition from Depth-to-Surface Filtration and Chapter 7 - Cake Filtration with a Composite Micro-Nanofiber Filter. Unfortunately, it is not straightforward to answer these questions and even a full-blown 3D numerical model may not be able to simulate some of these phenomena and make logical interpretations of the numerical results to answer the forementioned questions. Therefore we adopt a two-dimensional (2D) model as a quick start to address these issues. There are obvious shortcomings and limitations, but the approach and outcome may warrant such an approach as a start in favor of a 3D numerical model where numerical results may be difficult to interpret and generalize.

Because of unsatisfactory models and limited measurements in air filtration, numerical simulation is widely utilized to gain an understanding on dynamic dendritic growth, and thus the time-dependent capture efficiency and pressure drop during aerosol filtration. To solve these problems a numerical method will be developed to simulate polydispersed nanoaerosol deposition, including depth filtration, cake formation on a nanofiber filter, and the transition between these two regimes. The pressure drop, filtration efficiency, cake porosity, and the effect of aerosol number concentration challenging a nanofiber filter will be investigated. Although flow through aerosol dendrites is intrinsically 3D, 3D simulation of aerosol loading a filter is very expensive and complex. Hence, a special 2D approach is considered herein as a kick-off to simulating the unsteady-state air filtration on submicron- and nanoaerosols. Flow field calculations and aerosol tracking have been performed using the Fluent CFD code enhanced with in-house C++ subroutines.

Powder Technology
Journal

Chemical Engineering Journal
Journal

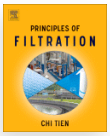

Principles of Filtration
Book • 2012

From other publishers

Journal of Organic Chemistry
Journal

Organometallics
Journal

Journal of Asian Natural Products
Journal

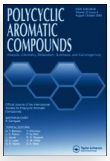

Polycyclic Aromatic Compounds
Journal